N Eidietis et al.

The ITPA Disuprion Database

The ITPA Disruption Database

N.W. Eidietis[1], S.P. Gerhardt[2], R.S Granetz[3], Y. Kawano[4], M. Lehnen[5],
G. Pautasso[6], V. Riccardo[7], R.L. Tanna[8], A.J. Thornton[7],
ITPA Disruption Database Participants and JET EFDA contributors*

JET-EFDA, Culham Science Centre, OX14 3DB, Abingdon, UK

[1]*General Atomics, P.O. Box 85608, San Diego, California 92186-5608, USA*
[2]*Princeton Plasma Physics Laboratory, Princeton NJ, 08543, USA*
[3]*MIT Plasma Science and Fusion Center, Cambridge, MA 02139, USA*
[4]*Japan Atomic Energy Agency, Ibaraki 311-0193, Japan*
[5]*ITER Organization, Route de Vinon sur Verdon, 13115 St Paul Lez Durance, France*
[6]*Max-Planck-Institut fur Plasmaphysik, EURATOM Association, D-85748 Garching, Germany*
[7]*CCFE, Culham Science Centre, Abingdon, Oxon, OX14 3DB, UK*
[8]*Institute for Plasma Research, Bhat, Gandhinagar 382428, India*
* See annex of F. Romanelli et al, "Overview of JET Results",
(24th IAEA Fusion Energy Conference, San Diego, USA (2012)).

ABSTRACT

A multi-device database of disruption characteristics has been developed under the auspices of the International Tokamak Physics Activity magneto-hydrodynamics topical group. The purpose of this ITPA Disruption Database (IDDB) is to find the commonalities between the disruption and disruption mitigation characteristics in a wide variety of tokamaks in order to elucidate the physics underlying tokamak disruptions and to extrapolate toward much larger devices, such as ITER and future burning plasma devices. In contrast to previous smaller disruption data collation efforts, the IDDB aims to provide significant context for each shot provided, allowing exploration of a wide array of relationships between pre-disruption and disruption parameters. The IDDB presently includes contributions from nine tokamaks, including both conventional aspect ratio and spherical tokamaks. An initial parametric analysis of the available data is presented. This analysis includes current quench rates, halo current fraction and peaking, and the effectiveness of massive impurity injection. The IDDB is publicly available, with instruction for access provided herein.

INTRODUCTION

Large instabilities can cause a tokamak discharge to rapidly terminate, releasing the stored thermal and magnetic energy in a sequence called a disruption [1]. The high heat flux and mechanical loads transmitted to the vessel during a disruption have the potential to erode the first wall and stress critical mechanical components [2,3]. In contemporary tokamaks the consequences of a disruption are typically relatively minor, and, when breakage does occur, repairs can be made in a timely manner. However, in ITER [4] and future burning plasma devices the electromagnetic pressure load on the vessel wall will increase by a factor ~ 3 over present devices, and the time-normalized surface energy loading to the divertor is expected to increase by almost an order of magnitude [5,6]. These increased loads could result in prompt mechanical failure of the in-vessel components [7] and significantly limit the lifetime of plasma facing components [8]. Given the highly activated nuclear environment of ITER, as well as its sheer size, repair of in-vessel components will be very costly, both in terms of lost time and expense.

The rapid injection of massive quantities of radiating impurities into the plasma can be used to mitigate the most virulent consequences of disruptions. This process converts the thermal and magnetic stored energy of the plasma into electromagnetic radiation in order to distribute the energy as isotropically as possible across the plasma facing components, minimizing localized thermal and mechanical loads. The most commonly used method for massive impurity injection is massive gas injection (MGI) [9-13], although various forms of impurity pellets have also been studied [14-17].

Understanding both how the effects of disruptions and the effectiveness of their mitigation will scale from present devices to a burning plasma device (e.g. ITER) will be critical for the design of such a device. Unfortunately, the combination of rapid time scales, highly non-linear processes, intense wall interaction, and large-scale impurity transport make comprehensive quantitative numerical predictions of disruption phenomena difficult. While individual aspects of the disruption

and mitigation processes have been modeled (see [18-22] for example), these models often require significant assumptions regarding the plasma state during the disruption, making accurate predictions difficult. An empirical database of disruption parameters is therefore desirable to complement and enhance the existing modeling efforts, as well as to provide empirical scaling where no viable model exists.

A multi-device disruption database has been developed under the auspices of the International Tokamak Physics Activity (ITPA) [23] magneto-hydrodynamics (MHD) stability topical group. The ITPA Disruption Database (IDDB) aims to illustrate the commonalities in disruption characteristics and mitigation over a wide variety of tokamaks. Contributing devices include the conventional aspect ratio tokamaks ADITYA [24,25], Alcator C-Mod [26], ASDEX Upgrade [27], DIII-D [28], JET [29], JT-60U [30], and TCV [31] as well as the spherical tokamaks (ST's) MAST [32] and NSTX [33]. The work described herein represents an expansion of the effort originally initiated in [34,35].

In contrast to previous smaller disruption data collation efforts [5,36], the IDDB aims to provide significant experimental context for each shot provided. This allows exploration of a wide array of parametric relationships between pre-disruption and disruption parameters rather than limiting the investigator to a small number of parameters chosen *a priori*. Sufficient provenance information is provided for identification and further detailed investigation of particularly interesting data points with the providing institutions.

The IDDB is made available for public access and research. This article presents an introduction to the IDDB and exposition of the available data, but it is not intended, nor able, to serve as an exhaustive reference for all the relationships that can be explored using the IDDB. Continued examination of IDDB data by interested parties is enabled and encouraged. Moreover, the IDDB is in a continuing state of development, and additional variables and data may be added as deemed necessary by the ITPA MHD topical group to better clarify physics. Devices wishing to join the IDDB effort or expand upon previous submissions may do so, as detailed in Section 4.

The remainder of this article is structured as follows. The structure and content of the IDDB is discussed in Section 2. An initial parametric analysis of the IDDB data is provided in Section 3. Details for gaining access to and participating in the IDDB are given in Section 4, followed by closing remarks in Section 5.

2. DATABASE DESCRIPTION
2.1 STRUCTURE OF THE DATABASE
Although it is formally structured as a single MDSPlus [37] database, the IDDB can be split into three conceptual tables: general plasma pre-disruptive and current quench characteristics, halo current, and massive impurity injection. The names and descriptions of the fields contained within the tables are listed in Tables A.1, A.2, and A.3 in Appendix A, respectively. Each record within the database corresponds to a unique shot.

All submitted disruptions (natural or otherwise) must include data for Table A.1. Shots with halo current information should include the data in Table A.1 and Table A.2 (and Table A.3, if mitigated). Shots with massive impurity injection must include the data in Tables A.1 and A.3. Due to the inevitable variation in diagnostic and analytic capability between devices, it is not possible for all devices to provide data for all fields within a given table. Therefore, only a subset of fields within each table, believed to be commonly available to most devices, are designated as critical and strongly requested in order to submit data to the table. Those fields are highlighted in the tables of Appendix A.

The IDDB experimental data is composed almost exclusively of scalar variables, as the decision was made early in IDDB development that the complexity of time-series data across such a large dataset would confuse, rather than clarify, subsequent analysis. Additional explanatory data is included as text fields.

Table A.1 includes provenance information for each shot, equilibrium information describing the pre-disruptive plasma, and characterization of the current quench. The provenance information includes the submitting device's name, shot number, and miscellaneous comments that allow the data record to be traced back to its source if more complete, time-dependent analysis is desired. The plasma geometric and kinetic data is reported at the time of the last acceptably converging equilibrium reconstruction (TIMEQD) before the onset of the disruption (TIMED). Those times, as well as key times during the current quench, are illustrated in Figure 1. Table A.2 describes the halo current resulting from a disruption, including both descriptions of the halo current itself as well as plasma parameters at the time of maximum halo current. The halo current time fields are also illustrated in Figure 1. Table A.3 describes massive impurity injection for disruption mitigation. One part of the table describes the inputs to the mitigation, including a specification of the hardware involved, the type and amount of impurity used, and the trigger timing. The second part of the table describes the outputs of the mitigation, including details of the radiated power and particle assimilation.

2.2 OVERVIEW OF CONTRIBUTING DEVICES

The numerous devices contributing to the IDDB provide a wide variety of operating parameters. Table 1 displays the ranges of select plasma parameters submitted by each device to the IDDB to illustrate this variety.

With the exception of Aditya, which is purely a circular limited configuration, all of the devices can operate in a diverted configuration, although some of the submitted data may be from limited plasmas. Excepting Aditya, all devices utilize a Grad-Shafranov equilibrium reconstruction code (e.g. EFIT [38]) to provide the IDDB plasma equilibrium parameters.

A majority of the contributing devices have provided halo current data to the IDDB. Comparing each halo current monitoring system is beyond the scope of this paper. However, salient references describing the halo current monitoring systems and providing in-depth device-specific analysis of the halo current data are listed in Table 2. Similarly, the injectors used for disruption mitigation by

massive impurity injection and the diagnostics and methods used to analyze the results differ from device to device. A listing of references for device-specific massive impurity injection data is also provided in Table 2.

2.3 DISTRIBUTION OF CONTRIBUTED DATA

The IDDB data population is not evenly distributed across topical categories or devices. Not all devices are capable of contributing to all sections of the IDDB due to diagnostic constraints. In addition, when data is available, the criteria utilized by each device to determine the number of shots that it provides to the IDDB varies greatly. This disparity in populations is illustrated Figure 2.

As can be seen in Figure 2a displaying the categorical distribution, the number of shots including halo current data (Table A.2) is over five times the number including massive impurity injection data (Table A.3), but both of those are only a minority of the total number of shots (including at least the basic data of Table A.1). This categorical disparity is a result of several factors. First, not all devices have the diagnostic capability or impurity injectors to provide halo current and/or impurity injection data. Second, while the basic disruption characterization and halo current measurements can largely be accomplished in the background, thereby providing data from almost every discharge, massive impurity injection is typically only utilized on dedicated run days, and as such represents a very small minority of a device's total discharges. Finally, the population disparity reflects the varying level of analysis required for each category. Collecting the basic plasma equilibrium and current quench data for Table A.1 is fairly straightforward and amenable to automation given that the necessary diagnostics and methods are critical to basic device operation and thus are almost always available and archived. Likewise, the halo current data, if available, is readily extracted via simple automated processes. In contrast, the massive impurity injection data (particularly regarding radiated power and time-dependent particle injection) require more intense analysis for each shot, resulting in a much lower rate of submission to the IDDB.

Figure 2b displays the relative contribution of each device to the total number of shots within each category. It is clear from this plot that the IDDB data is skewed towards a minority of devices. Alcator C-Mod, DIII-D, and JET dominate the total shot population (i.e. those discharges including data for at least Table A.1). The halo current distribution is more evenly distributed, although JET is the dominant contributor by almost a factor of two. The impurity injection data is largely dominated by Alcator C-Mod and DIII-D contributions. However, as the Alcator C-Mod data does not include radiated power or time-dependent particle injection components, the DIII-D contribution is by far the largest in the analysis presented in Section 3.3. Whenever possible in the analysis of Section 3, the data is separated by device in order to provide a visual indication of any disparities in population density that may be present.

The overlap of the IDDB data with ITER's nominal operating points also varies significantly. This is illustrated in Figure 3, which displays the relative distribution of (a) aspect ratio, (b) β_N, and (c) l_i in the IDDB versus the nominal ITER operating ranges given in [4]. The illustrated ITER

4

operating ranges include the expected values during flattop operation in the ITER inductive, hybrid, and steady-state scenarios [4]. These ranges would expand if the dynamic ramp-up and ramp-down phases of each scenario were included. As seen in Figure 3a, the IDDB aspect ratio distribution peaks almost exactly at the ITER value of A=3.1. In contrast, it is evident from the β_N distribution in Figure 3b that the IDDB contains dominantly low β_N plasmas compared to the ITER operating range ($\beta_N \approx$ 1.8-2.7), peaking at less than a third of the ITER range. The distribution of l_i shown in Figure 3c represents a middle ground, showing significant overlap with the ITER operating range but skewed towards more peaked current profiles than expected for ITER. These examples illustrate that the strength of the IDDB data is not in matching the ITER parameters, but rather for elucidating the physical models that will allow extrapolation to the ITER operating range.

3. DATABASE ANALYSIS

The following section presents select analyses of data available within the IDDB. It is not intended to represent an exhaustive discussion of IDDB data, but rather to illustrate the utility of the IDDB by presenting parametric relationships that have been of historic interest for characterizing tokamak disruptions and those relevant to the design of the ITER disruption mitigation system. Parameter names listed in CAPITAL letters refer to IDDB fields, which can be referenced in the tables of Appendix A.

3.1 TOROIDAL CURRENT QUENCH RATE

The rapid loss of toroidal current during the current quench (CQ) can induce significant eddy currents that can threaten the mechanical integrity of in-vessel components. It is necessary to place a lower bound on the expected current quench time (Δt_{cq}) in ITER to robustly design in-vessel components. The CQ rate is typically normalized by the plasma cross-sectional area (S, or AREAD in the IDDB) in order to better compare the CQ rates of disparate devices (Δt_{cqS}), as detailed in [36]. In [5], a database of non-circular conventional aspect ratio tokamaks estimated a lower bound for the linear area-normalized CQ time of 1.8 ms/m^2. However, the portion of the CQ in [5] used to derive the linear CQ rate differed from device to device. This limit was further refined and reduced in [34,35] to 1.67 ms/m^2, using a consistent linear current quench extrapolated time $\Delta t_{80-20} = t_{20}-t_{80}/0.6$, where t_{80} and t_{20} (TIME8 and TIME2) are the times where the toroidal current reaches 80% and 20% of its pre-disruptive value (IPD), respectively (see Figure 1). This limit corresponds to a $\Delta t_{80-20} =$ 36ms in ITER. ITER simulations with a prescribed linear current quench of that duration, as well as an equivalent exponential current quench (τ_{cq}=16ms), are the design basis for the ITER blanket module and vacuum vessel against the induced electromagnetic forces [7]. $\Delta t_{cqS} = 1.67$ ms/m^2 will be referred to as the "ITER minimum" in the discussion below.

The present IDDB current quench data, shown in Figure 4, largely confirms the analysis of [34,35], and as such does not introduce new limitations into the ITER design. The linear CQ time is calculated uniformly for all devices as $\Delta t_{cqS} = \Delta t_{80-20}/S$, as in [34,35]. Plotted versus toroidal

current density (j_p) in Figure 4a, the minimum Δt_{cqS} fall under 0.6 ms/m^2, far below the ITER minimum (indicated by the horizontal dashed line). However, the low A devices (MAST and NSTX) exhibit a distinctly shorter Δt_{cqS} distribution than the conventional A devices, which is made clearer by plotting Δt_{cqS} versus aspect ratio, as in Figure 4b. It was noted in [35,36] that the low-A and conventional distributions can be better equalized by an additional normalization of the area-normalized current quench time by the plasma self-inductance, L* = ln(8 R/a)-1.75, yielding the normalized time $\Delta t_{cqSL} = \Delta t_{80-20}$/(SL*). As shown in Figure 4c, this additional normalization signifcantly increases the overlap of the two populations, resulting in an almost identical lower bound to Δt_{cqSL} formed by the low-A and conventional-A devices. However, that lower bound falls below the specified ITER minimum Δt_{cqSL}.

The problematic region below the ITER minimum, populated only by MAST, NSTX, and DIII-D, is expanded and plotted versus j_p in Figure 4d. Following the arguments presented in [34], that region can be divided into two sub-regions, separated by the dotted line in Figure 4d that indicates the ratio of the minimum ITER current quench time to the maximum ITER current density (corresponding to the 15MA ITER operating point). The region above the dotted line represents a "safe zone", wherein the maximum forces and impulse on the ITER vessel due to induced eddy currents are expected to be the same or lower than those modeled for the extremum point in [7] (15MA, 1.67 ms/m^2), due to the ratio of the ITER-equivalent current to Δt_{cqSL} being smaller. Discharges in that region do not represent an increased electromechanical threat to ITER, and thus need not be incorporated into the expected minimum Δt_{cqSL}. The region below the dotted line is an "unsafe" zone, where the forces and impulse would be expected to be larger than the modeled point due to that ratio being larger. Restricting the discussion to only the conventional-A data (DIII-D), all but one of the data below the ITER minimum limit are in the "safe" zone, allowing them to be dismissed for the purpose of establishing the minimum expected current quench for a 15MA ITER discharge. As detailed in [34], the lone DIII-D datum in the "unsafe" zone comes from an exceptionally low squareness shape inaccessible to ITER, and is also ignored. By this analysis, the lowest expected Δt_{cqS} predicted by the IDDB for ITER remains 1.67 ms/m^2, as determined in [34]. If the low-A data below are also considered, there are numerous NSTX and MAST discharges in Figure 4d that fall into the "unsafe" zone, but that data is not used to set limits for the conventional-A ITER.

As noted in [39], Δt_{cqS} can change significantly depending upon which portion of the CQ is used as the reference. Figure 5 displays the cumulative fraction of shots with Δt_{cqS} below a given value. The fraction of current quenches falling below the minimum allowable duration increases to between 1-2% when the linear CQ time is calculated using either the early ($\Delta t_{80-50} = (t_{50}-t_{80})/0.3$) or late ($\Delta t_{50-20} = (t_{20}-t_{50})/0.3$) portion of the CQ. This indicates that a portion of the CQs exhibit a strong exponential behavior (fast early decay) or a slow early decay followed by a faster late decay. In [52], Δt_{100-70} is utilized to minimize any effect from runaway electron formation during the CQ. The IDDB does not include t_{100}, but a close approximation of it, $\Delta t_{90-70} = (t_{70}-t_{90})/0.2$, is also shown in Figure 5. Using this metric, the fraction of discharges with Δt_{cqS} shorter than the

6

ITER minimum rises to nearly 5%. Given the analysis of [7], wherein the linear and exponential waveforms produced similar electromechanical results in the ITER vessel and blanket modules, it is not expected that these short time-scale differences will matter significantly for the large ITER components with long time constants. However, as noted in [7], the design of smaller in-vessel components (e.g. antennae) with shorter time constants may be affected.

Figure 5 also reveals slightly skewed distributions for vertical displacement event (VDE) and massive impurity injection discharges. When only discharges positively identified as VDEs are considered within the conventional aspect ratio subset, the fractional occurrence of $\Delta t_{80-20}/S$ shorter than the ITER minimum increases by a factor of ~3, to slightly below 1%. However, this is likely reflecting the smaller population of identified VDE discharges in the IDDB versus the general population rather than true physical causes. The disruptions resulting from massive impurity injection (typically MGI) within the database do not represent the fastest CQs. The distribution of Δt_{cqS} for MGI discharges exhibits a more compact distribution than the non-MGI cases, with the longest $\Delta t_{80-20}/S < 10$ ms/m^2 and the shortest still exceeding the ITER minimum. That the "natural" disruptions exhibit a lower minimum in Δt_{cqS} compared to the MGI cases is likely due to the fact that the fastest IDDB current quenches occur in DIII-D, which has entirely carbon plasma facing components (PFC) that are known to emit significant amounts of carbon impurity into the plasma during the thermal quench (TQ) [62]. The distribution for natural disruptions skews significantly towards longer Δt_{cq} for beryllium first wall and tungsten divertor devices, as has recently been reported for the ITER-like wall in JET [46], and is expected to do so in ITER as well.

3.2 HALO CURRENT

Similar to the eddy currents induced during the CQ, the induction of open field line poloidal "halo" currents during a vertical displacement event (VDE) can expose in-vessel components to potentially damaging $J \times B$ forces [40]. The ratio of the maximum axisymmetric halo current ($I_{h,max}$, IHMAX in the IDDB) to the pre-disruption plasma current (I_{p0}) is termed the halo fraction, $F = I_{h,max}/I_{p0}$. The halo current also often exhibits a non-axisymmetric structure, which is captured in the toroidal peaking factor (TPF) [41]. The TPF is recorded at the time of maximum halo current in the IDDB (TPFATMAX), as illustrated in Figure 1. The product F*TPF gives a measure of the maximum local poloidal halo current density within the vessel as a function of the pre-disruptive Ip.

The measurements of I_h and TPF are dependent upon both the toroidal resolution of the halo current sensors in a given device and the structure of the halo current asymmetry. For a system of N toroidally distributed poloidal halo current monitors each measuring a poloidal halo current density $j_{halo,n}$ (A/rad), the IDDB standard definitions of the axisymmetric halo current I_h and TPF are

$$I_h = 2\pi \frac{\sum_N^1 j_{halo,n}}{N} \tag{1}$$

and

$$TPF = \frac{\max\left(j_{halo,n}\right)}{I_h/2\pi}$$ (2)

where the maximum function represents the largest poloidal halo current density measured at a discrete toroidal location. The accuracy of these definitions depends upon toroidal mode structure of the halo current asymmetry and the ability of the halo current sensors to resolve it. Equation 1 is accurate so long as the spatial resolution of the halo current sensors is sufficient to avoid aliasing the actual halo current mode structure (i.e. an n=1 mode structure requires two sensors separated by 180° toroidally). If, as observed in [56], the asymmetry resembles a toroidally localized "lobe" rather than an n=1 mode, a high toroidal resolution is required to avoid aliasing. The measurement of the TPF (Equation 2) depends upon both the same aliasing constraint as I_h as well as the phase of the halo asymmetry. For example, even if two sensors sampling an n=1 asymmetry can accurately measure I_h, the measured TPF will depend upon whether the mode phase is orientated with its extrema or nodes located at the sensors, yielding TPF=2 or TPF=1, respectively.

The present IDDB F*TPF distribution, displayed in Figure 6, is qualitatively similar to previous results but with important quantitative differences for ITER. The bounding maximum value is F*TPF = 0.75, similar to that reported in [36] but exceeding the value of 0.7 reported in [5, 6]. This bounding value ignores two outlier points from Alcator C-Mod (dashed circle in Figure 6). Those outliers were found to occur late during an I_p and B_t ramp-down, inflating the halo fraction calculation and for that reason were not included in establishing the F*TPF limit. In addition, there are two JET discharges at F > 0.58 (solid circle in Figure 6), exceeding the previous limit of F < 0.52 in [5,6,36]. This new bound may have important engineering implications for ITER, as the maximum F is a critical design point in determining operational limits. Upon closer examination, both of these points were found to be measured by only a single toroidally localized halo current sensor. As noted above, a single sensor would alias any toroidal asymmetry, convoluting F and TPF. Thus, it is possible that the extreme halo fraction presented by the two points is the result of such aliasing and does not represent a new halo fraction limit for ITER. Further analysis of the discharges in question is required to make that determination.

The probability of a discharge reaching a given F*TPF value in the IDDB falls off rapidly as F*TPF increases. Figure 7 displays the cumulative probability of F*TPF for a given shot within the database exceeding a given value. Globally, the probability of an event exceeding F*TPF=0.6 is only ~1%, and exceeding F*TPF=0.7 is less than 0.2%. This IDDB probability is almost certainly an overestimate of the actual probability, as typically IDDB participants established a minimum threshold for halo current when choosing halo current measurements to submit, significantly skewing the database towards higher halo current fractions. For ITER, the actual probability of extreme events will likely be much lower.

It should be noted that the IDDB low-A F∗TPF distribution does not include many of the extreme points reported for MAST in [51]. This is due to a change in the MAST halo current analysis to avoid unwarranted distortions in F∗TPF. The MAST halo current monitor system includes detectors at various poloidal locations. In [51], the largest single halo fraction measured at any of those poloidal locations was multiplied by the TPF at all the locations, even though the locations with largest F may have recorded low TPF. This led to a skewing of the data towards large F∗TPF. In the present MAST IDDB data, F∗TPF is derived only from the measurement with the largest halo fraction., avoiding such distortion.

It was noted in [53] that the maximum F∗TPF in JET decreases with an increasing value of the pre-disruptive edge safety factor, q_{95}. A cross-device comparison shown in Figure 8 indicates that this is a global trend, with all devices exhibiting a downward trend in the maximum observed F∗TPF as the pre-disruptive q_{95} increases. This is consistent with the axisymmetric halo current model presented in [18], which states that the poloidal halo current is strongly dependent upon the edge safety factor, with lower safety factors producing a larger fraction of poloidal halo current. This is a positive result for ITER, as it indicates that the maximum expected halo current in the lower I_p ITER operating scenarios (hybrid, steady-state), as well as during the ramp-up and ramp-down periods of every shot, will not simply be reduced linearly in I_p relative to the 15 MA ITER inductive baseline flattop (i.e. F I_p falls linearly with I_p, for constant F), but also benefit from a reduction in F itself due to increased q_{95}.

In contrast, the observation in [53] that JET F∗TPF decreases with increasing current decay rate does not appear to be well supported within the IDDB. As shown in Figure 9, JET F∗TPF maximum exhibits a non-monotonic behavior, peaking around 50 s^{-1} and falling off to either side. NSTX exhibits a monotonic increase in the maximum F∗TPF as the current decay rate increases. MAST maintains fairly consistent values over a wide range of decay rate, and the other devices fail to exhibit any identifiable structure. A significant hidden variable may be the variation in the vertical displacement growth rate of the plasmas, which is not recorded in the IDDB, as F is strongly determined by the ratio of the current decay rate to the vertical displacement growth rate [18].

A reduction in halo fraction as the thermal energy (W_{th}) of the pre-disruptive plasma increases, observed in NSTX [47] and JT-60U [48], is not globally supported by IDDB data. This effect is attributed to an increase in impurity density due to increased conducted heat flux to the divertor, which in turn cools the halo region, makes it more resistive, and reduces the total halo current [48,53]. However, as shown in Figure 10, this is not a consistent trend across devices. Although NSTX does exhibit a reduction in the maximum F as W_{th} increases (JT-60U W_{th} is not available for the halo current measurements presently available in the IDDB), the trend is not consistent in other devices.

There are several factors that may be contributing to this discrepancy. The first is the material of the plasma facing components (PFC), in particular the divertor. For example, DIII-D and NSTX are both all-carbon devices and exhibit a general, if weak (in the case of DIII-D), reduction in F as

W_{th} increases. In contrast, Alcator C-Mod (molybdenum) and ASDEX-Upgrade (tungsten) exhibit no noticeable trend. This may indicate a much higher heat flux threshold for the high-Z metal wall material to pollute and cool the halo region as compared to carbon, making W_{th} unimportant for determining the halo fraction until that threshold might be reached. However, the carbon-wall data from MAST and JET (all JET halo current data presently in IDDB pre-dates the JET ITER-like wall upgrade [50]) also fail to follow the NSTX trend, indicating that other factors in addition to wall material also play a role. The second factor that should play a role is the distribution of the heat flux during a VDE, which is a function of the plasma and device geometry. This may explain the different trends between the two ST's, as NSTX has a simple open divertor [47], whereas MAST possesses a more intricate internal structure that provides multiple points of contact (of varying material) for the plasma boundary during a VDE [51]. With its beryllium wall and tungsten divertor, ITER is likely to behave more akin to the present metal wall devices (little relationship between F and W_{th}) than NSTX, and should not expect the benefit of decreasing F as W_{th} increases.

3.3 MASSIVE IMPURITY INJECTION

3.3.1 Cooling time

The cooling time, Δt_{cool}, between the arrival of injected impurities at the plasma edge and the onset of the current quench has implications for both the response time of the ITER DMS as well as the assimilation fraction of the injected impurities [52]. For the present discussion, $\Delta t_{cool} =$ TIMESPK – TIMPARRIV, using the current spike as a functional indicator of the end of the TQ phase. The arrival time of the impurities at the plasma boundary, TIMPARRIV, is measured slightly differently in each device, but is typically derived from the rapid rise in appropriately placed filterscopes or fast bolometer channels.

The relationship between Δt_{cool} and the number of atoms injected prior to the current spike ($N_{inj-spk}$, which is NPARTSPK multiplied by the number of atoms per molecule) is subject to significant uncertainty, but that can be reduced at ITER-relevant quantities by focusing upon neon injection. Numerous devices have observed that the TQ is initiated by the arrival of the impurity cooling front reaching the q=2 surface [60,61,63,65]. In addition, it was shown in [36] that the TQ duration scales linearly with the plasma minor radius (a). Both of these findings suggest that the plasma minor radius should be used to normalize an inter-device comparison of Δt_{cool}. In addition, it was shown in [64] that Δt_{cool} increases steadily with increasing q_{95}, which was attributed to the increasing distance of the q=2 surface from the plasma edge as q_{95} increased. Thus normalization by q_{95} is also warranted. In Figure 11, Δt_{cool}, normalized by both the plasma minor radius (AMIND) and q_{95} (Q95D), Δt_{cool*}, is plotted versus $N_{inj-spk}$, separated by device (Figure 11a) and impurity species (Figure 11b). $N_{inj-spk}$ is normalized to the vessel volume (V_{vessel}) to provide comparison between disparate devices. The maximum possible ITER normalized injection quantity, corresponding to 8 kPa-m^3 impurity gas *all* injected prior to the current spike, is indicated by the vertical dashed line.

Figure 11 displays a consistent weak decrease in the minimum Δt_{cool*} over a wide range of

$N_{inj-spk}$ (as reported in [52]). However, the scatter in Δt_{cool*} is roughly an order of magnitude at any given injection value, including the ITER maximum. The floor of the distribution is dominated by the pure high-Z impurities (Ar, Ne) as well as He mixed with high-Z impurities. He mixtures, typically a large majority He with a minority of high-Z atoms (ratio specified by SPECIESRAT), are utilized to entrain the slow sound-speed high-Z impurities within the much faster flow of the He atoms, enabling significantly faster delivery of the high-Z radiators [57]. In Figure 11b, it is evident that these mixtures, even with a minority of high-Z radiators as low as 10%, can result in Δt_{cool*} matching even the pure high-Z radiators.

The spread in Δt_{cool*} is significantly reduced if the analysis is restricted to only neon, a likely candidate for the ITER radiating species. As indicated by the red dotted line in Figure 11b, a reasonable ceiling on Δt_{cool*} can be established, indicating $\Delta t_{cool*} < 1.22$ ms/m at the maximum ITER injection capability and increasing steadily below that level of impurity injection. Taking the ITER inductive baseline scenario $q_{95}=3.1$ and a=2.2 m, this corresponds to a maximum $\Delta t_{cool} < 8.3$ms for the maximum possible ITER neon injection.

A lower bound for the expected ITER Δt_{cool} can be established by comparing Δt_{cool} to W_{th}. It is reasonable to expect that, all else being constant, increasing W_{th} would require increasing Δt_{cool} to cool the plasma enough to induce the violent resistive MHD that brings on the thermal quench. However, [52] indicates that this trend is saturated for large injection quantities. A comparison of Δt_{cool*} to $W_{th}/N_{inj-spk}$ (a measure of the plasma thermal energy available to each impurity atom) across devices provides a broader view (Figure 12). The minimum ITER $W_{th}/N_{inj-spk}$ corresponding to nominal baseline scenario flattop operation ($W_{th}=350$MJ, 8 kPa-m^3 injected prior to current spike) is indicated by the dashed vertical line. While there is significant scatter in Δt_{cool*}, a clear lower bound appears at a given $W_{th}/N_{inj-spk}$, indicated by the dotted red line in Figure 12b. That lower bound increases monotonically with W_{th} (or decreasing $N_{inj-spk}$). It is set by the pure high-Z radiators (Ne and Ar) and high-Z mixtures (Figure 12b), as is expected. This lower bound appears to asymptote at very low values of $W_{th}/N_{inj-spk}$ (< 0.1 keV/atom), but those are over an order of magnitude below the ITER minimum. At the ITER minimum, the bound is $\Delta t_{cool*} > 1$ ms/m, and the bound increases slowly as $N_{inj-spk}$ decreases. Assuming the same ITER equilibrium values as above, this corresponds to a minimum $\Delta t_{cool} > 6.8$ ms at the maximum possible ITER neon injection capability.

The large degree of scatter in Figures 11 and 12 likely comes from two sources. First, it is indicative of numerous hidden variables that obscure the simple two-parameter relationship. A primary purpose of the IDDB is to clearly identify these points of ambiguity (which may not be obvious from controlled, single machine experiments) and provide the necessary context to gradually extract more complete & general multi-variable relationships. This strongly motivates further multi-variable regression analysis of the IDDB data to reveal further significant variables. A second source of the scatter may be the calculation of $N_{inj-spk}$ itself. $N_{inj-spk}$ is subject to significant uncertainty, as no device has a direct measurement of this quantity. Each device utilizes its own methods for

estimating the time-dependent flow rate of its MGI valves (annotated in MNPARTSPK). Typically, analytic models of varying complexity are utilized, such as described in [58] for DIII-D valves, [59] for the MAST & JET valve design, and [12] for AUG. JT-60U uses a fast vessel pressure measurement. The combination of the indirect nature of the methods to obtain $N_{inj-spk}$, as well as the variety of methods used between devices, may contribute to the observed data spread in Figure 11 and Figure 12 and any other parametric comparison involving $N_{inj-spk}$.

3.3.2 Fueling efficiency

The effectiveness of an impurity injector is largely a function of its ability to get impurity particles across the plasma boundary, both to act as radiators of the plasma thermal and magnetic energy and to provide high electron density for runaway electron suppression. The ability to transport impurity ions into the core is measured by the fueling efficiency, here defined as $f_{inj} = N_e/N_{inj} =$ (DENSSPK5-DENS) VOLD / N_{inj}, where N_e is the total number of free electrons in the CQ plasma averaged between the current spike and the 50% current level. This definition of f_{inj} measures the efficiency creating free electrons during a disruption, and is equivalent to F_{eff} from [60], also used in [13], which is readily measured by multiple devices. This is in contrast to the fueling efficiency Y_{mix} defined in [62], which utilizes estimates of the average impurity charge state during the CQ to calculate the impurity ion population in the plasma, and therefore directly measures the ion assimilation. However, this second technique requires complex spectroscopic techniques to resolve the ion charge state, and hence is not included within the IDDB at this time.

Figure 13 displays f_{inj} as a function of W_{th} per the total number of injected impurity atoms (N_{inj}). Consistent with the results in [62], the overall trend shows increasing maximum f_{inj} as W_{th}/N_{inj} increases, which appears consistent across impurity species (although there are a small number of outlier points using He, which possesses the fastest sound speed of all the impurities). This is likely due to a convolution of the increased ionization capacity of the plasma (more energy per atom available to convert neutrals into ions) and the trend of increasing Δt_{cool} with increasing W_{th} per atom shown in Figure 12, which allows more time for impurity atoms to enter the plasma boundary before the TQ cools the plasma and limits further ionization. At the ITER minimum W_{th}/N_{inj} (indicated by the vertical dashed line in Figure 13), the expected maximum f_{inj} is ~0.3-0.4. However, due to the large scatter, it is not clear if that maximum will actually be achieved.

3.3.3. Radiated Energy Fraction

One of the primary purposes of disruption mitigation by massive impurity injection is to isotropically radiate the stored thermal energy of a disrupting plasma before the TQ occurs and conducts the thermal energy to highly localized portions of the vessel wall. The effectiveness of this radiation process can be measured by the thermal energy radiation fraction, $f_{th} = W_{rad-spk}/W_{th}$, where $W_{rad-spk}$ (WRAD_SPK) is the energy radiated between the time of impurity arrival at the plasma edge (TIMPARRIV) and the time of the current spike (TIMESPK), and W_{th} is the plasma stored thermal

energy (WTOTD). This definition assumes that minimal plasma magnetic energy is dissipated by the rapid radiation process before the CQ. Figure 14 shows that f_{th} is relatively insensitive to the thermal energy density of the plasma, consistent with data presented in [44,52,63]. $f_{th} = 1$ is attainable at all thermal energy densities presented, although the wide distribution of f_{th} indicates that such high radiation fraction is by no means guaranteed. The only noticeable trend in Figure 14 is an increasing population of f_{th} much greater than unity at low thermal energy densities. This due to the fact that at low W_{th} the assumptions in the definition of f_{th} break down, and the magnetic energy radiated prior to the current quench becomes a significant contributor to $W_{rad-spk}$, as noted in []. The trend in Figure 14 indicates the $f_{th} = 1$ may be accessible to ITER. However, this requires significant extrapolation from the thermal energy densities of the available dataset (< 80 kJ/m^3) to the ITER baseline flattop value (~ 420 kJ/m^3).

4. ACCESS TO IDDB

Public access and up-to-date information on the IDDB is available through the IDDB web site [67]. The active database is contained in a restricted access MDSPlus database maintained by General Atomics. Parties wishing to contribute additional data the to IDDB should reference [67] for data submission instructions. A publicly available version of the database is provided for global access. Instructions for obtaining access to the public version of the IDDB can be found at [67]. Any usage of the data contained within the public database should provide this article as reference, per ITPA database guidelines.

CONCLUSIONS

The ITPA MHD topical group has developed a multi-device disruption database characterizing tokamak disruptions and their mitigation. The IDDB provides a large number of parameters describing the pre-disruptive plasma, current quench, halo current, and mitigation by massive impurity injection. This context allows a wide variety of parametric relationships to be tested across the highly varied selection of participating devices, including both conventional and low aspect ratio tokamaks. The IDDB can be used to assess the generality of single-device results, re-assess previous multi-device parametric studies, and look for new relationships to provide scalings extrapolating to ITER and other large tokamaks.

Initial analysis of the present IDDB current quench data indicates that the previously accepted lower limit for area-normalized linear current quench in conventional aspect ratio devices of 1.67 ms/m^2 is still valid. The IDDB halo current data suggests an increase of the upper limit for halo current F*TPF from 0.7 to 0.75. In addition, the upper boundary in halo fraction has increased from ~0.52 to 0.58, but further analysis is required to determine whether a change in the ITER boundary is warranted given the ambiguities associated with the new measurements. Measurements of the cooling time during massive impurity injection provide rough bounds to the minimum and maximum expected cooling times in ITER, providing a window of ~6-9 ms assuming 100% assimilation of

injected neon particles prior to the current quench. Fueling efficiency data indicates that the actual ITER assimilation will be < 50%, which would slide the cooling time window towards longer durations. Large scatter in the data motivates further multi-variable analysis to refine the results.

The IDDB is in a continuing state of development. A public "frozen" version of the IDDB is made available, allowing for continued analysis of the available data beyond that presented in Section 3. Future planned additions to the database that would significantly expand the analysis of existing data include measurements of the growth rate of the vertical displacement during VDEs and measurements of the thermal quench onset time. Devices wishing to contribute additional data to the IDDB should refer to [67].

REFERENCES

[1]. Schuller F.C. 1995 *Plasma Physics and Controlled Fusion* **37** A135

[2]. Nygren R. *et al* 1997 *J. Nucl. Mater* **241-243** 522-527

[3]. Riccardo V. *et al* 2000 *Nuclear Fusion* **40** 1805-1810

[4]. Shimada M. *et al* 2007 *Nuclear Fusion* **47** S1-S17

[5]. Sugihara M. *et al* 2004 Proc. Of 20th IAEA Fusion Energy Conference, Villamoura, Portugal, Paper IT/P3-29

[6]. Hender T.C., Wesley J.C. *et al* 2007 *Nuclear Fusion* **47** S128-S202

[7]. Sugihara M., Shimada M. *et al* 2007 *Nuclear Fusion* **47** 337-352

[8]. Parker R.R 2000 *Nuclear Fusion* **40** 473

[9]. Whyte D.G., Jernigan T.C. *et al* 2003 *Journal of Nuclear Materials* **313-316** 1239-1246

[10]. Riccardo V. *et al* 2003 *Plasma Physics and Controlled Fusion* **45** A269–A284

[11]. Finken K.H. *et al* 2003 *Journal of Nuclear Materials* **313–316** 1247

[12]. Pautasso G. *et al* 2007 *Nuclear Fusion* **47** 900–913

[13]. Thornton A.J. et al 2012 *Plasma Physics and Controlled Fusion* **54** 125007

[14]. Pautasso G. *et al* 1996 *Nuclear Fusion* **36** 1291

[15]. Evans T.E. *et al* 1997 *ournal of Nuclear Materials* **241-243** 606-611

[16]. Hollmann E.M. *et al* 2010 *Physics of Plasmas* **17** 056117

[17]. Commaux N. *et al* 2010 *Nuclear Fusion* **50** 112001

[18]. Humphreys D.A. and Kellman A.G. 1999 *Physics of Plasmas* **6** 2742-2756

[19]. Paccagnella R. *et al* 2005 *Fusion Engineering and Design* **75–79** 589–593

[20]. Strauss H. *et al* 2013 *Nuclear Fusion* **53** 073018

[21]. Izzo V.A. 2006 *Nuclear Fusion* **46** 541–547

[22]. Izzo V.A. 2013 *Physics of Plasmas* **20** 056107

[23]. http://www.iter.org/org/team/fst/itpa/mhd

[24]. Bhatt S.B. *et al* 1989 *Indian Journal of Pure & Applied Physics*. **27** 710-742

[25]. Bora D. *et al* 2002 *Brazilian Journal of Phys*. **32** 193-216

[26]. Hutchinson I.H. *et al* 1994 *Physics of Plasmas* **1** 1511

[27]. Stroth *et al* 2013 *Nuclear Fusion* **53** 104003

[28]. Luxon J.L. 2002 *Nuclear Fusion* **42** 614–633

[29]. Romanelli F. and JET EFDA Contributors 2013 *Nucl*. *Fusion* **53** 104002

[30]. Isayama A. for the JT-60 Team 2011 *Nuclear Fusion* **51** 094010

[31]. S. Coda for the TCV Team 2013 *Nuclear Fusion* **53** 104011

[32]. Meyer H. *et al* 2013 *Nuclear Fusion* **53** 104008

[33]. Kaye S. et al 1999 *Fusion Technology* **36** 16–37

[34]. Wesley J.C. *et al* 2006 Proc. of 21st IAEA Fusion Energy Conference, Chengdu, China, Paper IT/P1-21

[35]. Wesley J.C. *et al* 2010 Proc. of 23rd IAEA Fusion Energy Conference, Daejon, South Korea, Paper IT/P1-26

[36]. MDSplus System, http://www.mdsplus.org/

[37]. Lao L.L. *et al* 1985 *Nuclear Fusion* **25** 1611

[38]. Riccardo V. *et al* 2005 *Plasma Physics and Controlled Fusion* **47** 117–129

[39]. Strait E.J. et al 1991 *Nuclear Fusion* **31** 527-534

[40]. Granetz R.S. *et al* 1996 *Nuclear Fusion* *36* 545-556

[41]. Granetz R.S. *et al* 2006 *Nuclear Fusion* **46** 1001

[42]. Granetz R.S. *et al* 2007 *Nuclear Fusion* **47** 1086

[43]. Pautasso G. *et al* 2011 *Nuclear Fusion* **51** 103009

[44]. Pautasso G. *et al* 2011 *Nuclear Fusion* **51** 043010

[45]. Lehnen M. *et al* 2013 *Nuclear Fusion* **53** 093007

[46]. Gerhardt S.P. *et al* 2012 *Nuclear Fusion* **52** 063005

[47]. Neyatani Y. *et al* 1999 *Nuclear Fusion* **39** 559-567

[48]. Bakhtiari M. *et al* 2005 *Nuclear Fusion* **45** 318–325

[49]. de Vries P.C. *et al* 2012 *Plasma Physics and Controlled Fusion* **54** 124032

[50]. Counsell G.F. *et al* 2007 *Plasma Physics and Controlled Fusion* **49** 435–446

[51]. Lehnen M. *et al* 2011 *Nuclear Fusion* **51** 123010

[52]. Riccardo V. *et al* 2004 *Plasma Physics of Controlled Fusion* **46** 925–934

[53]. Riccardo V. *et al* 2009 *Nuclear Fusion* **49** 055012

[54]. Gerhardt S.P. *et al* 2011 *Review of Scientific Instruments* **82**, 103502

[55]. Gerhardt S.P. *et al* 2013 *Nuclear Fusion* **53** 023005

[56]. Bakhtiari M. *et al* 2011) *Nuclear Fusion* **51** 063007

[57]. Hollmann E.M. *et al* 2008 *Contribution to Plasma Physics* **48** 260–264

[58]. Bozhenkov S.A. *et al* 2011 *Nuclear Fusion* **51** 083033

[59]. Pautasso G. *et al* 2009 *Plasma Physics of Controlled Fusion* **51** 124056

[60]. Thornton A.J. *et al* 2012 *Nuclear Fusion* **52** 063018

[61]. Hollmann E.M *et al* 2008 *Nuclear Fusion* **48** 115007

[62]. Hollmann E.M. *et al* 2005 *Nuclear Fusion* **45** 1046–1055

[63]. Hollmann E.M. *et al* 2007 *Physics of Plasmas* **14**, 012502

[64]. Bozhenkov S.A. *et al* 2008 *Plasma Physics of Controlled Fusion* **50** 105007

[65]. ITER Physics Guidelines, N 19 FDR 1 (01-06-07) R 0.2

[66]. https://fusion.gat.com/itpa-ddb/Home/

APPENDIX A: TABLES OF IDDB VARIABLES

Name	Unit	Data Type	Description
*AMIND	m	float	Minor radius
*AREAD	m^2	float	Poloidal cros-sectional area
BEPMHD_D		float	Poloidal beta at TIMED
BETAND	%-m-T/MA	float	Normalized toroidal beta at TIMED
BETANMAX	%-m-T/MA	float	Maximum betan measured at TIME
BETMHD_D	%	float	Toroidal beta at TIMED
BOUNDRD	m	float	Radial dimensions of plasma boundary at TIMED
BOUNDZD	m	float	Vertical dimensions of plasma boundary at TIMED
BPOLD	T	float	Average poloidal field around plasma cross-sectional surface at TIMED
BTD	T	float	Vacuum toroidal field at RGEOD at TIMED
CAUSED		string	Proximate cause of disruption (Internal, External)
CHISQD		float	chi-sq equilibrium fitting parameter
COMMENT		string	
CONFIGD		string	Plasma shape configuration: LIM, LSN,USN,DN, etc.
DATE		integer	Data of discharge. Format = yyyymmdd
DATAPROBLEM		integer	Flag indicating problems with part of data. Data should only be used with caution. 0 or empty = OK; >0=Problem, details noted in COMMENT
DATAIGNORE		integer	Flag indicating if data record is erroneous and should be ignored. 0 or empty = OK; >0= Ignore data, details noted in COMMENT
DELTALD		float	Lower triangularity at TIMED
DELTAUD		float	Upper triangularity at TIMED
DIDTMAX	A/s	float	Smoothed dI/dt measured at TIMEDIDTMAX
DIVNAME		string	Machine-specific divertor configuration: ADP, RDP, etc -
DRSEPD	m	float	Outer midplane radial distance between surfaces defined by upper and lower x-points at TIMED
ELM_E		string	ELMing at TIMEQD: Y or N
EVIDRAE_E		string	Evidence of runaways seen? Y or N
INDENTD		float	Beanlike indentation at TIMED
*INTLID		float	Internal inductance (l_i1) at TIMED
*IPD	A	float	Plasma current at TIMED
*IPEQD	A	float	Plasma current at TIMEQD
IPPHASED		string	Plasma current mode at TIMED: FLATTOP, RAMPUP, ETC.
IPSPK	A	float	Max current spike measured at TIMESPK
IPSPK_E		string	Discernable current spike? Y or N
IPT	A, s	signal	Plasma current through disruption (time series)
*KAPPAD		float	Elongation at TIMEQD (closest eq to TIMED)
NINDXD		float	Vertical stability critical index
PHASED		string	Performance mode at TIMEQD: O(hmic), H, L, Hyb, etc.
*Q95D		float	Safety factor at 95% flux at TIMED
QMIND		float	Minimum safety factor in plasma at TIMED
RGEOD	m	float	Plasma geometric center major radius at TIMED
*RMAGD	m	float	Plasma magnetic center major radius at TIMED
*SHOT		integer	Shot Number
SQUOD		float	Plasma upper, outer squareness at TIMED
SQUID		float	Plasma upper, inner squareness at TIMED
SQLOD		float	Plasma lower, outer squareness at TIMED
SQLID		float	Plasma lower, inner squareness at TIMED
TIME	s	float	Time of maximum performance in shot

Table A.1: Base IDDB Variables (= Required)*

TIME1	s	float	Time Ip falls to 10% of IPD
*TIME2	s	float	Time Ip falls to 20% of IPD
TIME3	s	float	Time Ip falls to 30% of IPD
TIME4	s	float	Time Ip falls to 40% of IPD
TIME5	s	float	Time Ip falls to 50% of IPD
TIME6	s	float	Time Ip falls to 60% of IPD
TIME7	s	float	Time Ip falls to 70% of IPD
*TIME8	s	float	Time Ip falls to 80% of IPD
TIME9	s	float	Time Ip falls to 90% of IPD
TIME95MAX	s	float	Time betan reaches 95% of BETANMAX
*TIMED	s	float	Typically 2 ms before current spike max dI/dt
TIMEDIDTMAX	s	float	Time of max increasing dI/dt
TIMEQD	s	float	Time of acceptable chisq EFIT closest to TIMED
TIMERMAX	s	float	Time of maximum radiated power
TIMESPK	s	float	Time of current max after TIMEDIDTMAX
*TOK		string	Tokamak name, e.g. "D3D","JET", etc...
TQ_E		string	Thermal quench data exist? Y or N
*VDE_E		string	Significant vertical motion before or during disruption? Y or N
*VDEDRIFT		string	Direction of vertical drift: UP, DN, NO[NE]
VOLD	m^3	float	Plasma volume at TIMED
WDIAD	J	float	Diamagnetic derived energy at TIMED
WTOTD	J	float	Total kinetic energy at TIMED
*ZMAGD	m	float	Plasma magnetic center height above midplane at TIMED

Table A.1: Base IDDB Variables (= Required) (Continued)*

Tag Name	Unit	Data Type	Description
*IHMAX	A	float	Maximum total in-vessel halo current (poloidal/vertical)
*TIMEIHM	s	float	Time of IHMAX
*TPFATMAX		float	Maximum localized halo current (A/rad)/toroidally-averaged halo current
*IPATMAX	A	float	Total plasma current (core + halo) at time of IHMAX
RATMAX	m	float	Major radius at time of IHMAX
ZATMAX	m	float	Height (Z-Z0) at time of IHMAX
KATMAX		float	Vertical elongation (b/a) at time of IHMAX
TIME	N	float	Peak vertical force on VV
TIMEFZM	s	float	Time of peak FZVV
IZVV	N*s	float	Total VV Z impulse (integral Fz dt)

Table A.2: Halo Current Variables (= Required)*

Tag Name	Unit	Data Type	Description
VVESSEL	m^3	float	Volume of the vacuum vessel
AVESSEL	m^2	float	Surface area of first wall (Including port holes)
INJTYPE[1,2]		string	Type of injector (VALVE: electromagnetic, piezo, guiding tube, etc.) or (PELLET: solid, shell, SPI,etc..)
INJDIST[1,2]	m^3	float	Distance valve to separatrix
INJANGPOL[1,2]	deg	float	Poloidal angle of injector location (counter-clockwise from outer midplane)
INJANGTOR[1,2]	deg	float	Toroidal angle of injector location
NPARTMAX[1,2]	1	float	Maximum possible number of particles that can be injected with this valve
PRESSMAX[1,2]	Pa	float	Maximum possible pressure [N/A for pellets]
PRESS[1,2]	Pa	float	Pressure in valve [N/A for pellets]
NPART[1,2]	1	float	Total number of injected particles (molecules, not atoms)
SPECIESMAJ[1,2]		string	Injected gas species (majority)
SPECIESMIN[1,2]		string	Injected gas species (minority)
SPECIESRAT[1,2]		float	Ratio majority / minority (particles)
NPARTSPK[1,2]		float	Number of particles injected at time TIMESPK (molecules, not atoms)
MNPARTSPK[1,2]		string	Method to determine NPARTICLE_SPK (gas flow modelling, lab calibration, etc)
TINJTRIG[1,2]	s	float	Time of valve trigger
TIMPARRIV	s	float	Time of impurity arrival at plasma edge (from visible, bolometry, edge temperature, other)
MIMPARRIV		string	Method to determine TIMPARRIV
DIDTMIN	A/s	float	Minimum negative dI/dt during current quench (max current drop)
TDIDTMIN	s	float	Time of minimum negative dI/dt
IPDIDTMIN	A	float	Plasma current at TIMEDIDTMIN
PRAD_MAX	W	float	Maximum radiated power at time TIMERMAX
WRAD	J	float	Total radiated energy during disruption (from TIMPARRIV to \TIME1)
WRAD_SPK	J	float	Radiated energy until TIMESPK
PRADASYM		float	Radiation asymmetry (max/min) at time TIMERMAX
PRADASYMANG[1,2]	Deg	float	Toroidal angle of radiated power measurement
DENS	m^-3	float	Central line-averaged density at TIMPARRIV
DENSSPK5	m^-3	float	Time-averaged line-averaged density from TIMESPK to TIME5
DENSMAXCQ	m^-3	float	Maximum central line-averaged density during current quench
TE	eV	float	Maximum electron temperature at TIMPARRIV
TI	eV	float	Maximum ion temperature at TIMPARRIV
TEPED	eV	float	Pedestal or LCFS electron temperature at TIMPARRIV
WDIAPED	J	float	Pedestal energy at TIMPARRIV
WTH_Q2	J	float	Thermal energy inside q = 2 at time TIMPARRIV
CONTROLSHOT		float	Control shot # without mitigation for comparison

Table A.3 Impurity Injection Variables (= Required)*

Device	R (m)	A	κ	I_p (MA)
Aditya	0.72-0.84	3.1-5.0	Circular	0.05-0.09
Alcator C-Mod	0.54-0.70	2.9-5.5	1.0-2.0	0.22-2.02
ASDEX-Upgrade	1.50-1.69	3.1-4.2	1.2-2.0	0.60-1.16
DIII-D	1.28-3.09	2.6-5.7	0.8-2.3	0.13-2.39
JET	2.86-3.14	2.9-4.1	1.1-2.2	1.00-4.06
JT-60U	3.08-3.33	3.5-3.9	1.4-1.9	0.67-1.41
MAST	0.70-0.91	1.5-2.0	1.4-2.0	0.41-1.06
NSTX	0.38-0.99	1.4-2.1	1.4-2.7	0.36-1.20
TCV	0.86-0.89	3.6-4.1	1.2-2.4	0.08-0.61

Table 1: Parameter range of IDDB data, sorted by device.

Device	Halo Ref.	Massive Impurity Ref.
Alcator C-Mod	[42]	[9,43,44,58]
ASDEX-Upgrade	[45,46]	[12,45,61]
DIII-D	[41,15]	[9,16,17,63,64]
JET	[3,54,55]	[47,53]
JT-60U	[49]	[50]
MAST	[52]	[13,62]
NSTX	[48,56,57]	

Table 2: References for device-specific halo current and massive impurity injection data.
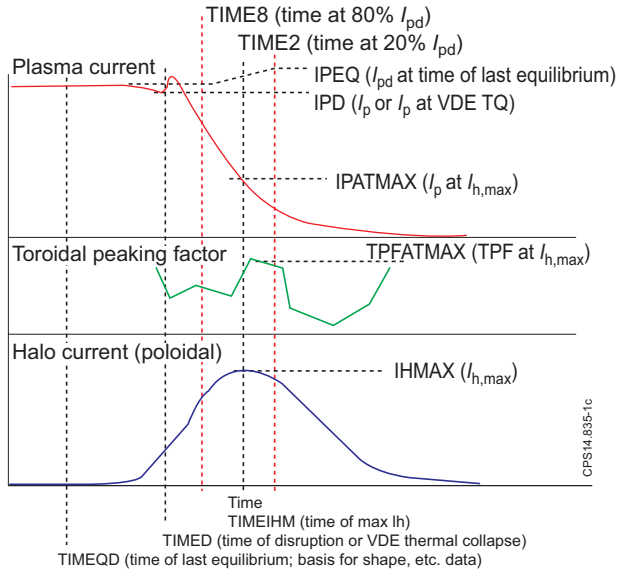
Figure 1: Illustration of key times within description of pre-disruptive plasma, current quench, and halo current evolution.
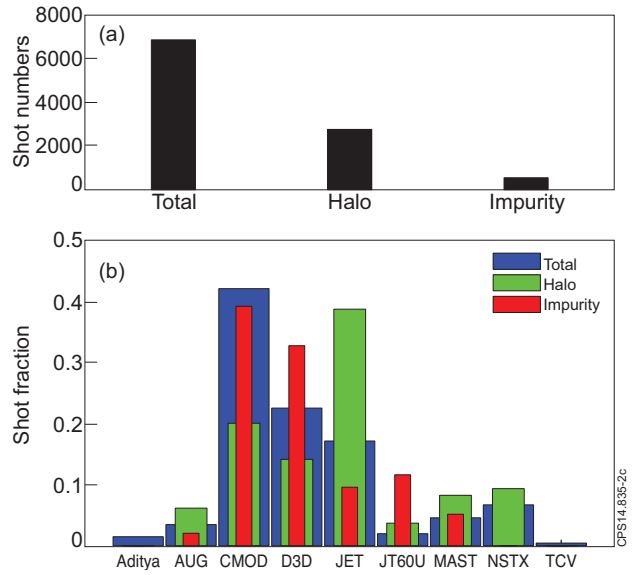
Figure 2: (a) Distribution of shots in IDDB, sorted by subcategory. (b) Fractional distribution of shots sorted by evice within each subcategory.
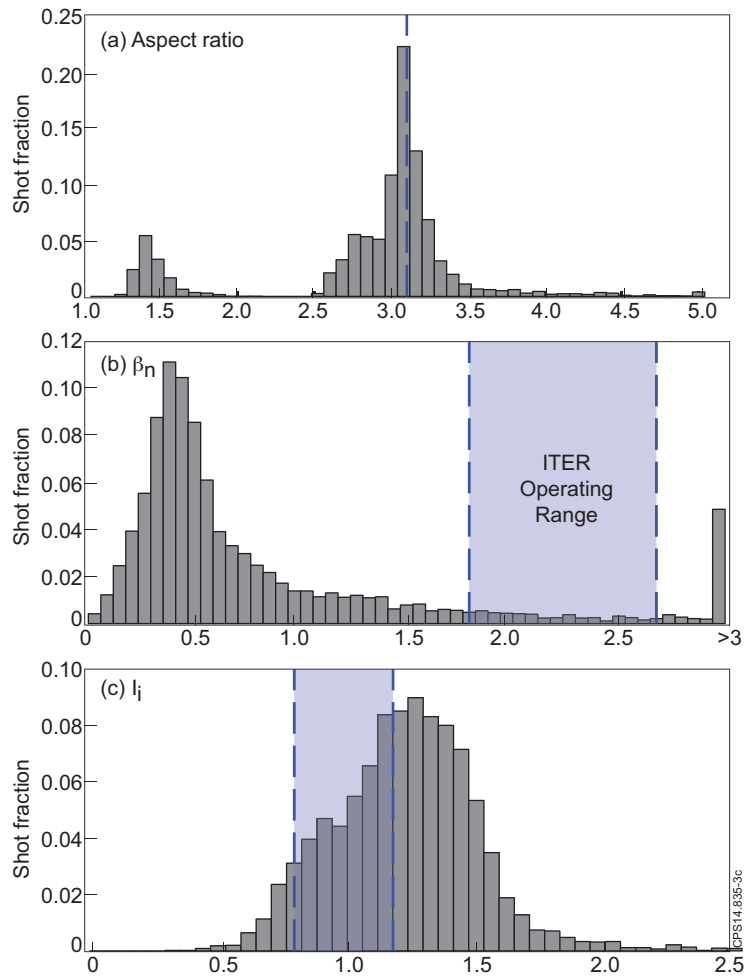
Figure 3: Distribution of select dimensionless variables in IDDB compared to nominal ITER flattop operating ranges, as listed in [4]. ITER ranges are indicated by shaded area between vertical dashed lines. Note that the ITER l_i values in [4] have been converted from the ITER standard $l_i(3)$ to $l_i(1)$ most commonly provided in the IDDB, per the definitions provided in the ITER Physics Guidelines [66].
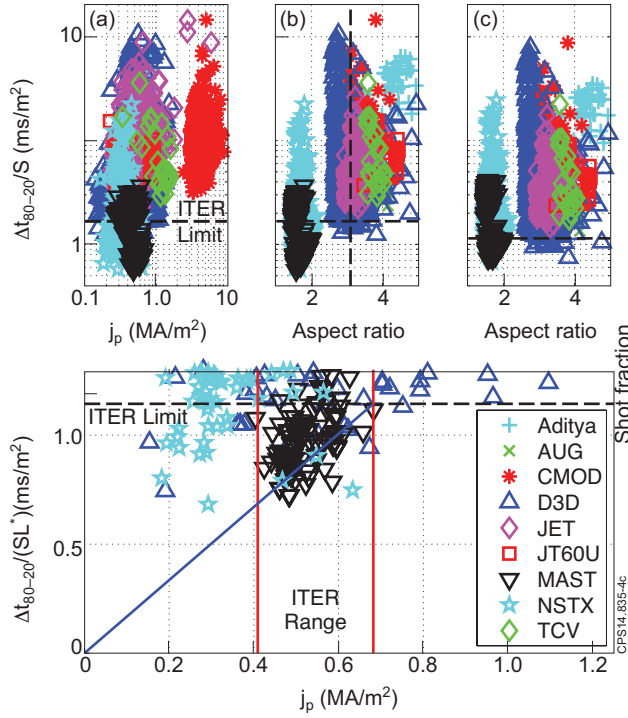
Figure 4: (a) Area normalized CQ duration versus toroidal current density (j_p), separated by device. (b) Area normalized CQ duration vs aspect ratio. (c) Additional normalization by the dimensionless self-inductance L* versus aspect ratio. (d) Magnification of area below ITER limit for area and L* normalized CQ duration versus j_p. The ITER flattop range of j_p is indicated by the vertical red lines. Black dashed line indicates the ITER minimum. Dotted blue line is an extrapolation to the ITER limit at the maximum ITER j_p.
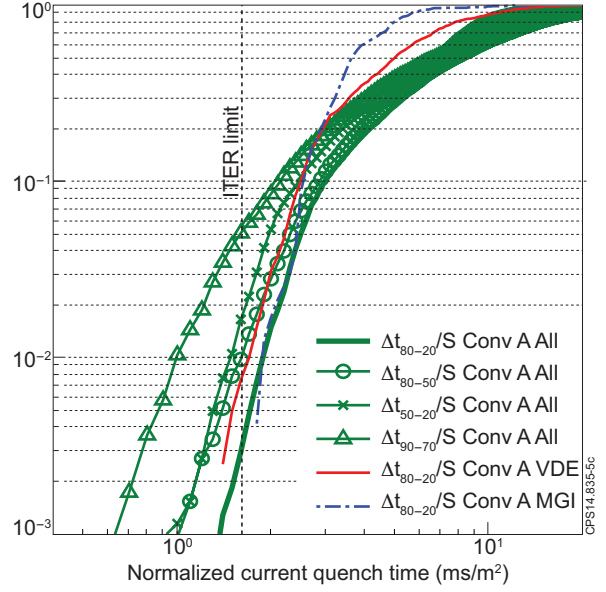
Figure 5: Cumulative probability of shot exhibiting an area-normalized CQ duration less than a given value, restricted to conventional-A devices. The minimum allowable value for ITER is indicated by vertical dashed line.
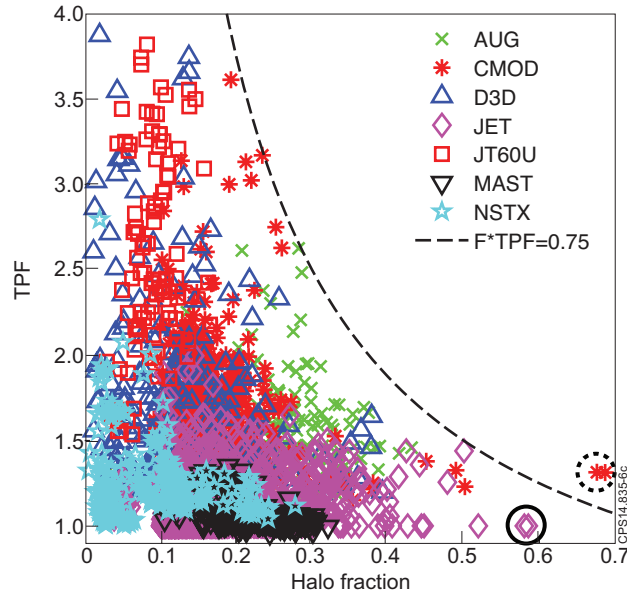
Figure 6: Toroidal peaking factor (TPF) versus halo fraction (F), separated by device. Dashed line indicates constant F*TPF = 0.75 boundary. The two cases exceeding F*TPF > 0.75 (dashed circle) occurred late in an I_p and B_t rampdown. The solid circled points represent an extension of the halo fraction boundary from previous data.
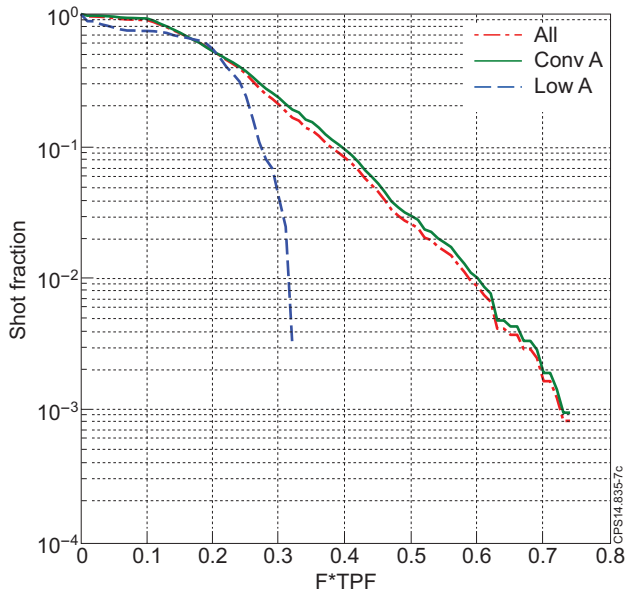
*Figure 7: Cumulative probability of F*TPF exceeding a given value. Shot populations are divided into all, low-A (MAST and NSTX), and conventional-A devices.*

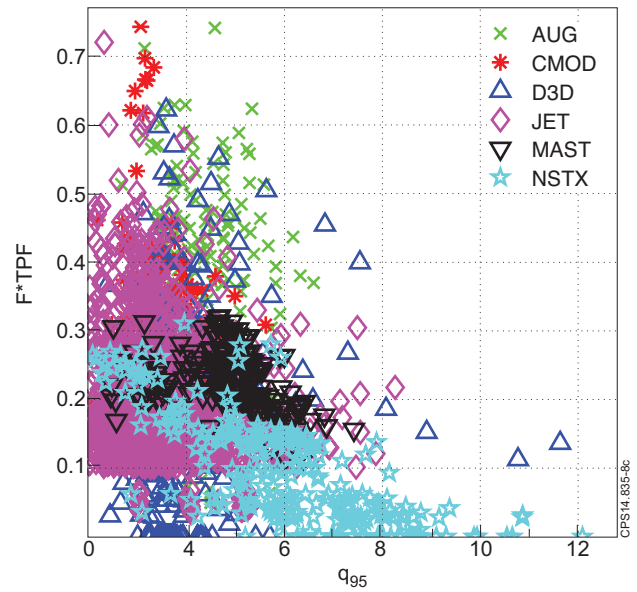*Figure 8: F*TPF versus q_{95}, separated by device.*

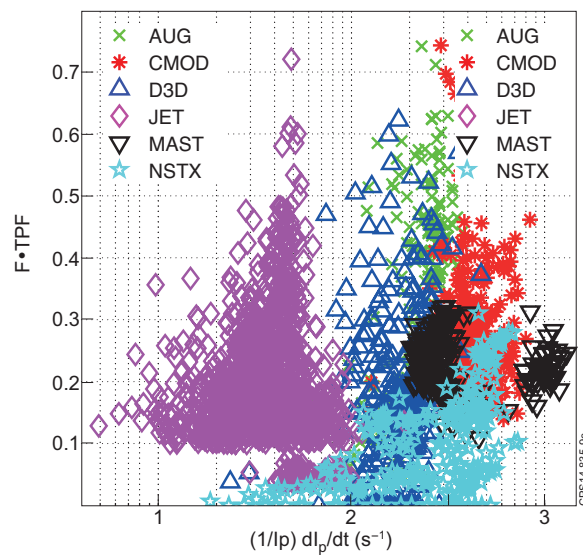*Figure 9: F•TPF vs current decay rate, separated by device. The current decay rate is given by $1/\Delta t_{80-20}$. The two distinct groups of MAST data correspond to lower-single null (faster decay group) and double null and upper single null (slower decay group) plasma shapes.*
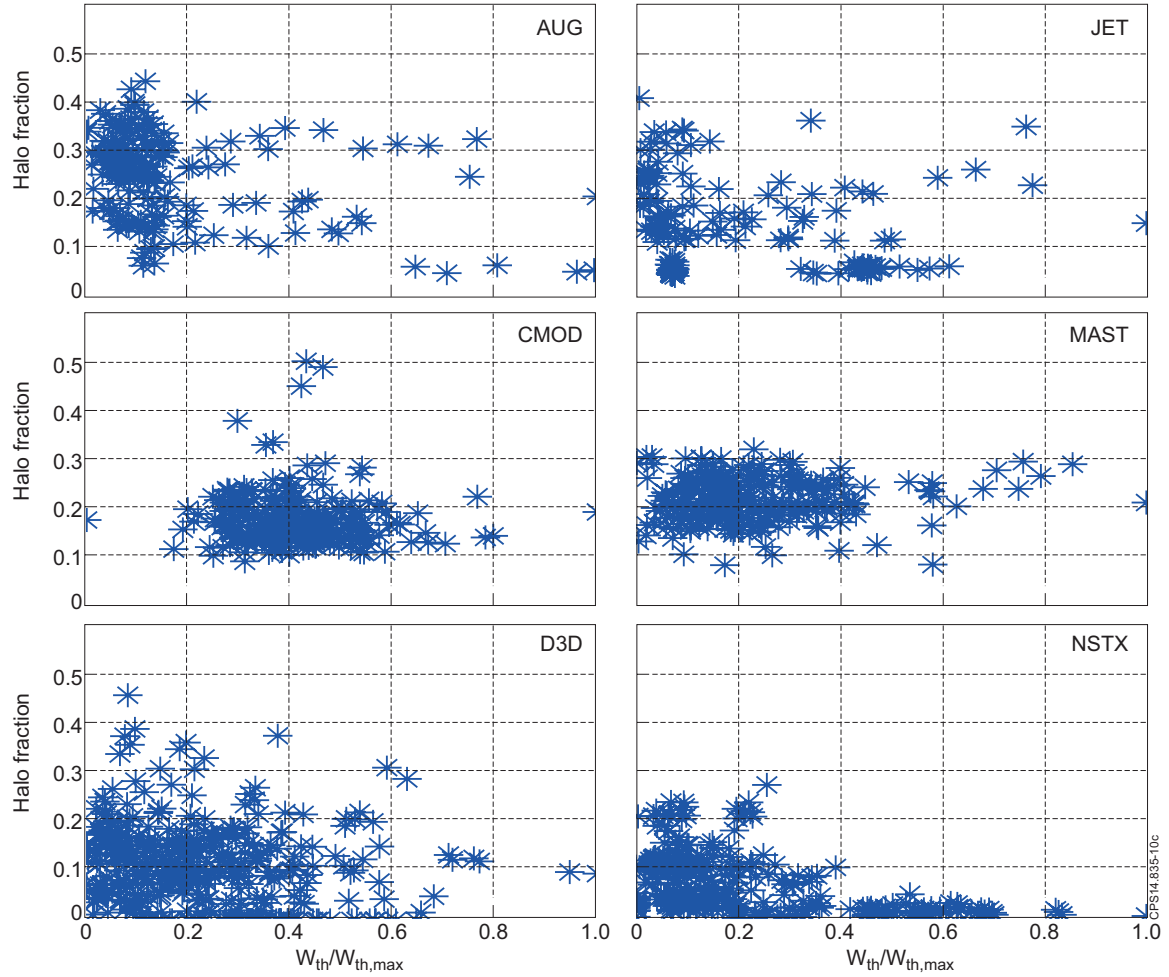
Figure 10: Comparison of F versus $W_{th}/W_{th,max}$, organized by device. $W_{th,max}$ is the maximum W_{th} reported by each device for the halo current data plotted.
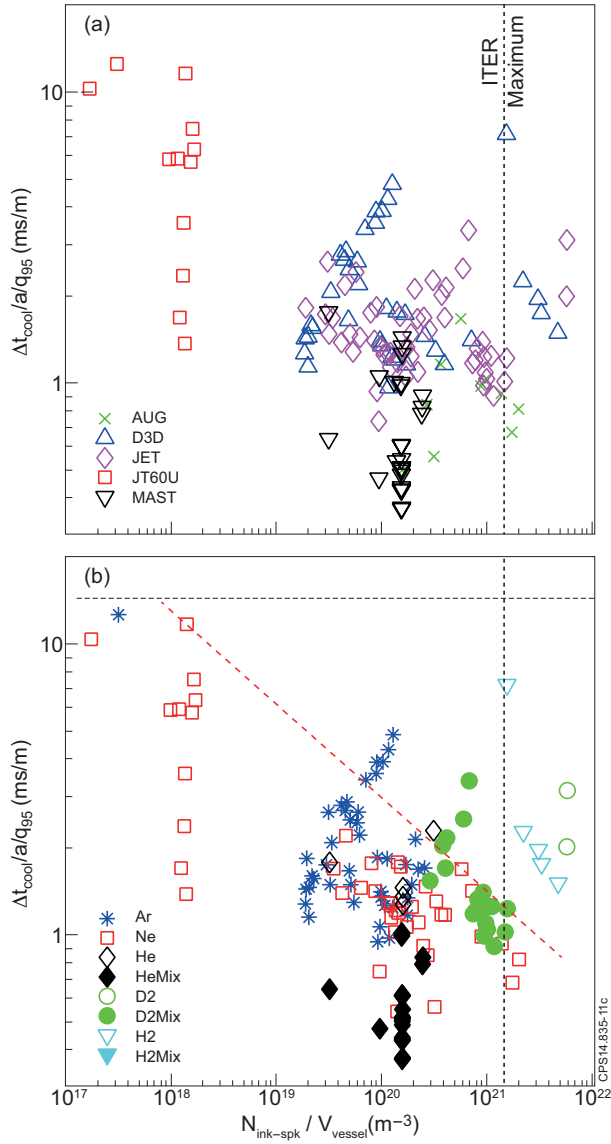
Figure 11: Normalized cooling time versus impurity atoms injected before the current spike, separated by device (a) and impurity species (b). Vertical dashed black line indicates maximum ITER injection capability, assuming all particles enter plasma before the current spike. Red dotted line indicates empirical upper limit for neon injection.
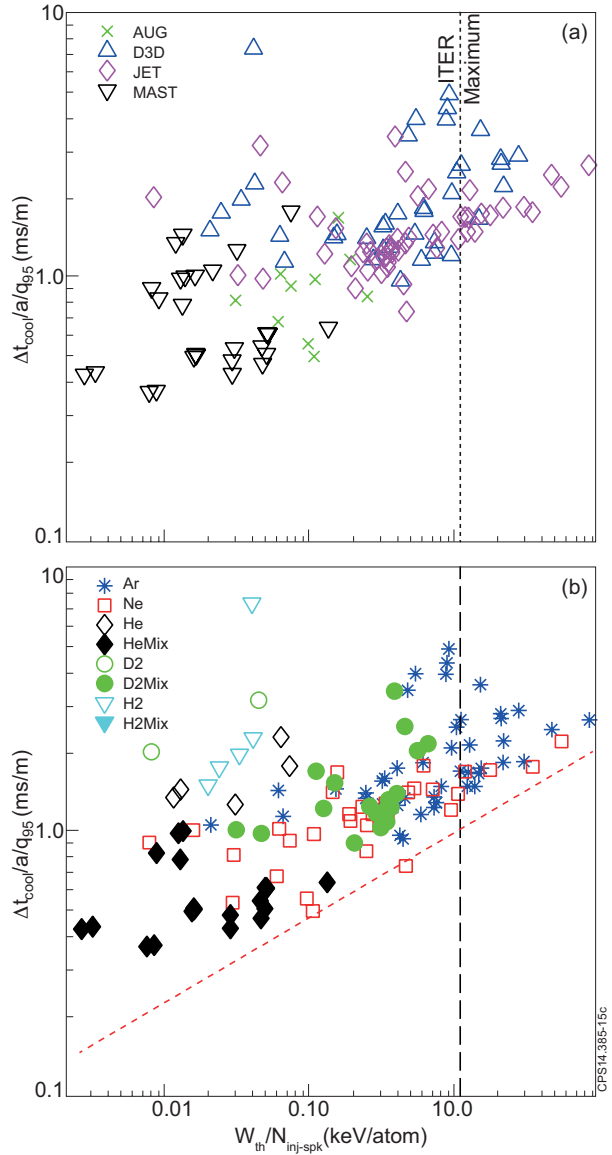
Figure 12: Normalized cooling time versus W_{th} per impurity atom injected before the current spike, separated by device (a), and impurity species (b). Vertical dashed black line indicates minimum value for ITER flattop operation. Red dotted line indicates empirical lower limit for neon injection.
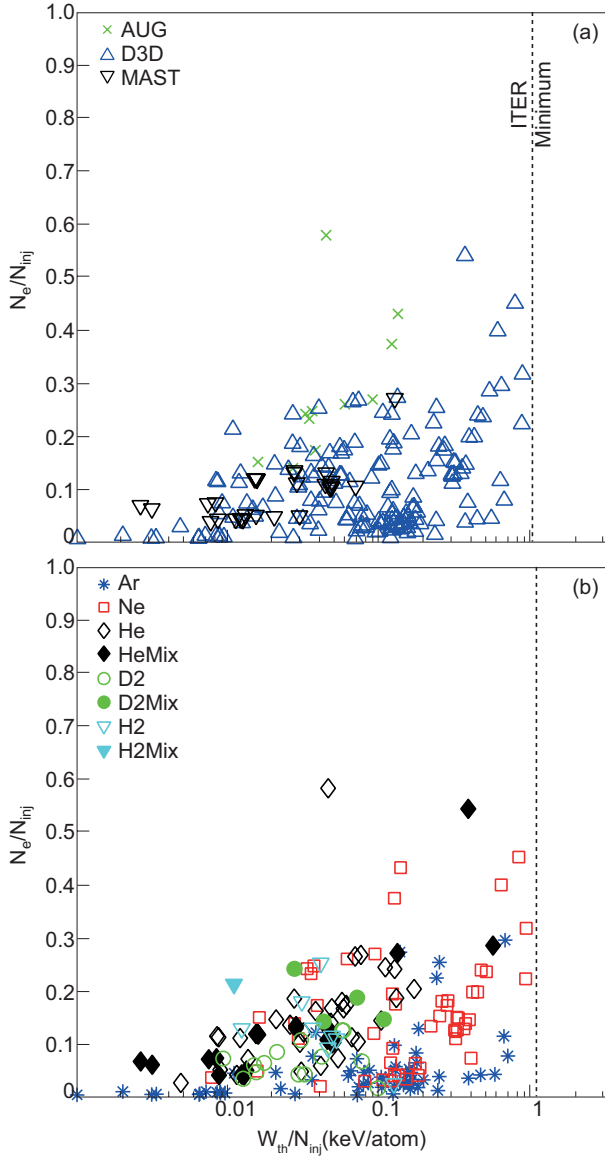
Figure 13: Fueling efficiency versus W_{th} per injected impurity atom, separated by device (a) and impurity species (b). Vertical dashed black line indicates minimum value for ITER flattop operation.
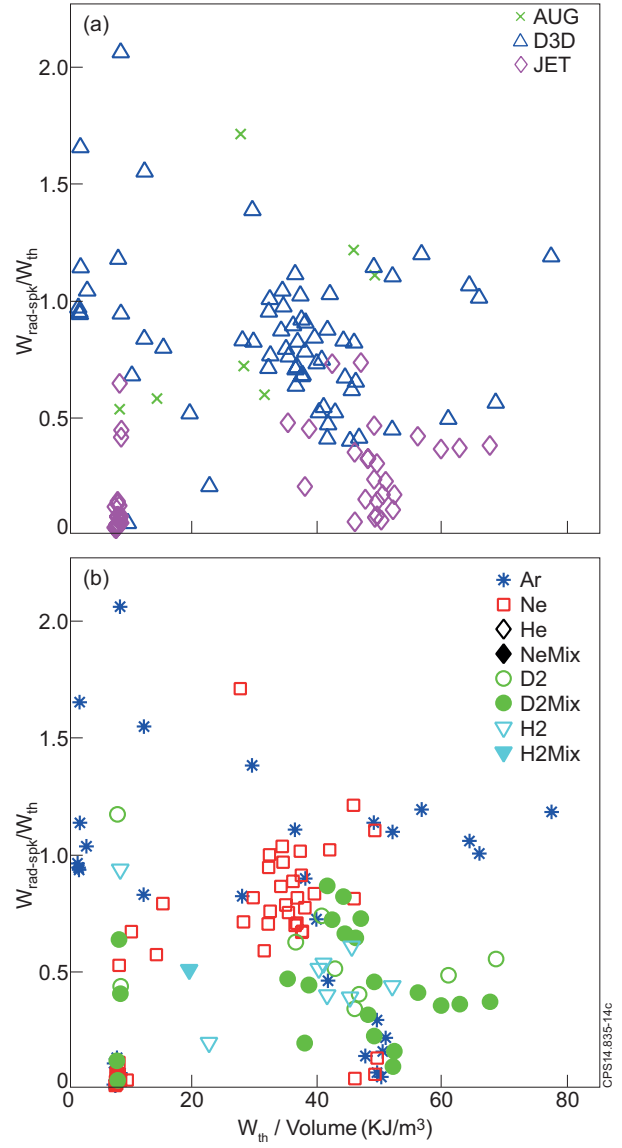
Figure 14: f_{th} versus thermal energy density, separated by device (a) and impurity species (b).